

# FRX-L: A Field-Reversed Configuration Plasma Injector for Magnetized Target Fusion

J. M. Taccetti, T. P. Intrator, G. A. Wurden, S. Y. Zhang, R. Aragonéz, P. N. Assmus, C. M. Bass, C. Carey, S. A. deVries, W. J. Fienup, I. Furno, S. C. Hsu, M. P. Kozar, M. C. Langner, J. Liang, R. J. Maqueda, R. A. Martinez, P. G. Sanchez, K. F. Schoenberg, K. J. Scott, R. E. Siemon, E. M. Tejero, E. H. Trask, M. Tuszewski, and W. J. Waganaar

*Los Alamos National Laboratory, Los Alamos, NM, 87545*

C. Grabowski, E. L. Ruden, J. H. Degnan, T. Cavazos, D. G. Gale, and W. Sommars

*Air Force Research Laboratory, Albuquerque, NM, 87117*

(Dated: May 9, 2003)

## Abstract

We describe the experiment and technology leading to a target plasma for the magnetized target fusion research effort, an approach to fusion wherein a plasma with embedded magnetic fields is formed and subsequently adiabatically compressed to fusion conditions. The target plasmas under consideration, field-reversed configurations (FRCs), have the required closed-field-line topology and are translatable and compressible. Our goal is to form high-density ( $10^{17} \text{ cm}^{-3}$ ) FRCs on the FRX-L (Field-Reversed eXperiment-Liner) device, inside a 36 cm long, 6.2 cm radius theta coil, with 5 T peak magnetic field and azimuthal electric field as high as 1 kV/cm. FRCs have been formed with an equilibrium density  $n_e \approx 1 - 2 \times 10^{16} \text{ cm}^{-3}$ ,  $T_e + T_i \approx 250 \text{ eV}$ , and excluded flux  $\approx 2\text{-}3 \text{ mWebers}$ .

PACS numbers: 52.55.Lf

## I. INTRODUCTION

FRX-L (Field-Reversed eXperiment-Liner) is a plasma formation experiment at Los Alamos National Laboratory, operated in collaboration with researchers from Air Force Research Laboratory. The principal goal of this experiment is to form and translate a field-reversed configuration (FRC) with  $T \approx 300$  eV,  $n \approx 10^{17}$  cm $^{-3}$ , and lifetime  $> 10$   $\mu$ s into a metallic liner (flux-conserving shell). This is a precursor to demonstrating an approach to fusion called Magnetized Target Fusion (MTF) [1]. The FRC has been selected as a promising candidate target plasma because of the large existing empirical database [2] and its proven ability to withstand translation and distortion [3].

MTF is an alternative approach to fusion that lies between the two more conventional approaches, Magnetic Fusion Energy (MFE) and Inertial Confinement Fusion (ICF), with respect to plasma lifetime and density. MFE timescales are long (milliseconds to hours) and initial densities are low ( $\approx 10^{12} - 10^{14}$  cm $^{-3}$ ). Magnetic fields are used to improve plasma confinement beyond that expected for the free-flight loss time. Some examples of this method are the tokamak, spheromak, stellarator, reversed-field pinch, etc. ICF lies at the other extreme of the spectrum. In ICF, fusion occurs during short times ( $\approx 10^{-9}$  s) but at high density ( $\approx 10^{24} - 10^{26}$  cm $^{-3}$ ), resulting in short pulses of high power. A pellet of fusion fuel is heated on its outer surface, and the expelled gases and radiation cause the outer shell to compress the inner fuel. The ICF approach does not require magnetic confinement and benefits from higher fusion reactivity at higher densities. However, ICF requires extremely high uniformity, not only in engineering of the pellet but also in the delivery of the heating to the pellet due to the high volume compression ratios required [4].

MTF combines advantages of ICF and MFE [5–8]. A target plasma with  $n \approx 10^{17} - 10^{19}$  cm $^{-3}$  is compressed, as in ICF, but is preheated and has magnetic fields embedded in it to insulate the plasma from the wall. Compared to ICF, this relaxes the requirements on compression uniformity and velocity—compression can take microseconds rather than nanoseconds. Fusion reactivity is given by the formula

$$R = n_D n_T \langle \sigma_{DT} v \rangle = \frac{1}{4} n^2 \langle \sigma_{DT} v \rangle, \quad (1)$$

where  $n_D$  and  $n_T$  are densities of deuterium and tritium,  $\langle \sigma_{DT} v \rangle$  is the average cross-section for a DT reaction, and we are assuming [9]  $n_D = n_T = n/2$ . As stated before, higher density improves the reaction rate by many orders of magnitude over conventional

MFE. Most characteristic plasma scale lengths also decrease with increasing plasma density, thereby decreasing system size with respect to MFE.

The MTF process—at least as it relates to FRX-L—can be separated into three distinct steps: formation of target plasma, translation of target plasma into target chamber (cylindrical liner, or ‘can’), and compression of the chamber along with the plasma to fusion conditions, coupling the compressional energy into the plasma (see Fig. 1). The MTF concept itself is more general and encompasses other target plasma and driver combinations, but the basic requirements for the target plasma are the same: a starting temperature of  $T_e \approx T_i \approx 50\text{--}300$  eV, a density of  $10^{17}$  cm $^{-3}$ , and a closed field line topology with a magnetic field of  $\approx 5$  T. The compression in our case is achieved by driving a large axial current along the liner. The liner implodes, or *pinches*, maintaining its shape, at least until the required radial compression factor is reached (10 times for our case) [10–12]. This adiabatic compression occurs at speeds on the order of cm/ $\mu$ s, which are easily achievable with existing pulsed-power facilities, such as the Shiva-Star facility at AFRL [13] or the Atlas facility under construction in Nevada (formerly at LANL) [14].

We chose to use the FRC as our target plasma because it has the required closed-field-line topology and has been shown to be translatable and compressible. The large existing empirical database gives us predictive capability and indicates that the type of FRC required for MTF is achievable [2]. FRX-L is used to form these FRCs and will translate them into a mock liner. We are currently studying the FRC formation process in the high-density regime.

An FRC is a toroidal plasma configuration with toroidal current and poloidal magnetic field, and ideally no toroidal field. It is composed of a closed field line region on the inside and an open field line region on the outside. If formed inside a theta coil (commonly known as the field-reversed theta pinch, or FRTP, method), the symmetry axis of the resulting FRC coincides with the axis of the theta coil, as can be seen in Fig. 1. The volume-averaged plasma beta (ratio of internal particle and field pressure to external field pressure) is approximately unity, the highest energy density plasma that can be confined for a given closed magnetic field structure. The open field line region serves as a natural divertor, allowing any particles which are able to escape the confined plasma region to do it along the axis rather than deposit their energy on the walls.

Although we use the FRTP method for FRC formation, there are various other ways to

do this [2]. The formation sequence is detailed in Sec. II along with a description of the FRX-L device.

For FRC-based MTF we require higher density FRCs than those formed by currently operating experiments—essentially returning to the kind of parameters seen in the early FRC experiments [2]. Although lifetime is thereby shortened, the plasma need only last long enough to be translated and compressed, or  $> 10 \mu\text{s}$ . Similar large  $E_\theta$  (kV/cm) FRCs have been produced in the past [15–19], but none have been done coupled with presently known cusp-formation techniques nor with the modern suite of diagnostics at our disposal [20, 21]. In addition, none were done with the intent of application to MTF, which presents its own set of unique requirements. These include stability during formation and compression, energy confinement adequate for fast liner compressional heating, liner-plasma interactions, and plasma impurity content and the general consequences of high-energy-density plasma-wall interactions.

## II. FRX-L EXPERIMENTAL DESCRIPTION

In this section we introduce the principal elements of the FRX-L experiment, including a description of the physical components, the electrical circuit and its operation, the vacuum system and related components, and control and data acquisition systems. An overview of the existing diagnostics follows, although specific diagnostic results are left for Sec. III.

The experimental design was guided principally by existing major hardware components (such as the main capacitor bank facility) coupled with future plans for integrated liner-on-plasma compression experiments. We begin by requiring fusion relevant conditions in the final plasma and work backwards from that point. We assume a possible  $10 \times$  compression of the aluminum liner, and use the energy of an existing liner compression capacitor bank (Shiva-Star at AFRL [13]) and fix the liner mass to pick a liner velocity that we can achieve. This in turn sets the liner size, which sets the plasma size and starting plasma density and pressure needed. A zero-D model for the cylindrical liner compression of the FRC [22, 23], and FRC semi-empirical formation models [24], were then used to determine required fields, which in turn drove the design of the coils and the electrical circuit. Table I summarizes the design parameters for the experiment and compares them to our actual parameters (see following sections for more details on how the latter were obtained).

## A. Physical Layout and Components

The FRX-L experiment is distributed among three rooms composing the experimental facility: the experimental bay, the screen room, and a workspace/test-area. The experimental bay contains all of the pulsed power components and the experimental vessel. Its high walls and interlocked doors protect personnel, who must remain outside during operation. We discuss the screen room further in Sec. II D.

Figure 2 is a top-view of the experimental bay, drawn to scale. The principal components of the experiment are indicated on the figure: the vacuum vessel (pump stand, quartz tube, and liner regions) and the electrical components (theta coil with transmission line, pre-ionization—or PI—bank, main bank, bias bank, and cusp/mirror bank and coils, as well as the stainless steel flux excluder plates between these and the theta coil). The locations of the power supplies and triggers are also shown for reference. Other equipment, such as the engineering controls used to return the capacitor banks to a safe state and the diagnostics, are not shown on this figure.

The central part of the machine is the theta coil, inside of which sits the quartz discharge tube. The coil is a single turn aluminum coil, segmented to allow access for diagnostics through three 1 cm gaps (Fig. 3). The current is fed into the theta coil via a parallel-plate transmission line made up of two 2.5-cm thick aluminum plates. These plates lie horizontally and are 36 cm wide at the theta coil side, widening to 2.5 m at the other end to accept 64 RG17/14 coaxial input cables. The top and bottom plates are insulated from each other with 24 layers of 127  $\mu\text{m}$  thick Mylar film. These many layers are necessary to minimize the possibility for imperfections in the Mylar allowing a direct tracking path from one plate to the other (in the section prior to the discharge tube). The Mylar sticks out 30 cm from the edges of the plates to prevent surface tracking. At the input side, the plates transition to coaxial cables over a distance of 30 cm. This transition region is covered by an airtight box into which  $\text{SF}_6$  is introduced to prevent breakdown during a shot (one machine cycle, consisting of charging capacitors, discharging them, and reading out data channels). The bias, PI, and main banks connect to the transmission line via the RG17/14 cables.

The bias bank consists of two FRX-C compression modules [25, 26] connected in parallel, mounted on top of each other. Each of these modules is composed of two General Electric 500  $\mu\text{F}$ , 10 kV capacitors in parallel. These are connected to a bias inductor (4  $\mu\text{H}$ ) with

copper bus bars to inductively isolate the bank from the PI and main bank discharges. The capacitors are charged with a Spellman SA10P4 10-kV power supply and are switched into the circuit using a water cooled ignitron (National Electronics NL-488A) on each module, triggered with North Star Research IG5-F2 ignitron triggers. The original FRX-C modules were modified slightly to charge negatively and yet maintain current in the same direction through the ignitrons, as is required for their operation.

The PI bank is made up of two Aerovox AeroStor  $1.35 \mu\text{F}$  100 kV capacitors. These are attached to a pair of parallel plates which lay horizontally on top of the capacitors. The plates are insulated from each other by 24 layers of  $127 \mu\text{m}$  thick Mylar. The plates were made to accommodate up to six capacitors in order to vary PI current and ringing frequency during pre-ionization. Presently we use two capacitors, resulting in a frequency  $f = 250 \text{ kHz}$ . The PI bank power supply is a Spellman SA70P4 70-kV supply, and the PI bank is switched using a single Maxwell pressurized rail-gap switch (Model 40 302 ‘Atlas-type’ [14]). The initial trigger is supplied by a Maxwell 40168 Trigger Amplifier that in turn triggers a Maxwell 40151B Trigger Generator. The latter supplies a 100-kV pulse to trigger the rail-gap switch. Similarly to the theta coil transmission line, an  $\text{SF}_6$  box surrounds the parallel plate to cable transition. Eight low-inductance RG17/14 cables connect the PI bank to the theta coil header.

The main capacitor bank (field-reversal bank) is a two-stage Marx bank with a maximum erected voltage of 120 kV. A Marx bank is a capacitor bank that is split into equal parts (two in our case) charged in parallel to the same potential. These are then switched in series or ‘erected’ such that their voltage multiplies by the number of stages. Since each half of our bank has a capacitance of  $72 \mu\text{F}$ , it becomes  $36 \mu\text{F}$  when erected. Two separate power supplies (Universal Voltronics HV DC Power Supply, BPO 62-800-LANL), one positive, the other negative, are used to charge the lower and upper half of the Marx bank, respectively. The bank is erected by and discharges through four Maxwell pressurized rail-gap switches (Model 40 302). Since the bank can provide up to 0.25 MJ, a protection circuit was designed to prevent against damage from a prefire that could cause a single switch to take all the energy [27]. If a prefire is detected, a signal is automatically sent to trigger the remaining three switches thereby sharing the current among all of them. The trigger system is similar to the one used for the PI bank.

The crowbar switch is identical to the one used to discharge the main bank but is situated

on the output side. The purpose of the crowbar is to extend the lifetime of the FRC by maintaining the current in the load relatively constant after it reaches its first peak. The design of the crowbar is described elsewhere [28].

The cusp bank is a separate circuit, though mutual inductance must be considered due to the close proximity of the cusp coils to the theta coil. Individual coils are 16-turn hollow copper conductor coils encased in epoxy, having a thickness of 2.5 cm and an ID of 14 cm. Three of these coils side by side combine to form a cusp coil. Stainless steel shield plates with a soak-through time  $\approx 100 \mu\text{s}$ , or flux excluders, are placed between these coils and the theta coil to reduce mutual inductance (the cusp field, with a quarter cycle time of  $900 \mu\text{s}$ , penetrates these, while the PI and main bank fields do not). The entire cusp bank consists of four FRX-C double modules, identical to the ones used on the bias bank. Four additional modules are available for when we increase the number of coils to include a set surrounding the liner region into which the FRC will be translated. The modules are powered by a Peter Dahl 10 kV supply.

## B. Vacuum System

The vacuum chamber consists primarily of an 11-cm outer diameter dielectric quartz tube of 2.5 mm wall thickness located inside the theta coil. The tube is evacuated and filled with deuterium at low pressure. The pump stand, supporting the mechanical and turbo pumps, is on a separate frame, and the pump manifold is connected to one end of the quartz tube via a bellows to reduce vibrations. (The other end of the quartz tube is where the liner will be located and into which the FRC will be translated in the near future.)

All vacuum flanges use copper gaskets except for the seal with the quartz tube. This seal was specially designed to deal with the varying tolerances of the quartz tube. Each seal is comprised of a Viton o-ring that fits around the tube at each end and specially shaped stainless rings that press on the o-ring from either side, compressing it against the quartz tube and making a seal. The base pressure in the vacuum chamber before a shot is approximately  $3 \times 10^{-7}$  Torr.

The working gas is deuterium,  $\text{D}_2$ . We operate with a static gas fill, with pressures ranging from 10 to 100 mTorr. Future plans include an upgrade to a puff fill system. The  $\text{D}_2$  fill line is maintained under positive pressure. When ready for a shot, a plenum of approximately

500 cm<sup>3</sup> is filled to a pressure on the order of a few Torr, after which the fill line valve is closed and the plenum is opened to the chamber.

The principal pump is a Varian TV-551 Navigator, 550 l/sec turbo pump, backed up by a dedicated mechanical pump. An independent mechanical pump is used to rough out the chamber prior to opening it to the turbo pump. An automatic vacuum control system using National Instruments Fieldpoint modules and LabVIEW Realtime software controls the various sequences and prevents damage to the vacuum components. All of the vacuum gauges are automatically disconnected during a shot via air-driven switches.

### C. Electrical Circuit and Operation

The FRX-L circuit consists basically of a theta-pinch coil (a straight coil, i.e. it has no mirror fields at the ends) driven by various capacitor banks in parallel, precisely timed to form, contain, and translate an FRC with the temperature, density, and lifetime appropriate for MTF. A simplified circuit diagram is shown on Fig. 4. Not all parasitic inductances and capacitances are shown on this diagram. The principal components, as shown, are the crowbar and the main, bias, and PI capacitor banks.

The formation sequence follows very closely the explanation presented by Hoffman *et al.* [29], except that our theta coil has no passive mirror. We instead use a separate set of slow cusp coils at either end of the theta coil, which null out the initial bias field at these locations (pull theta coil field lines radially outward), but later serve as mirrors with respect to the main bank reverse field. The following are details of the sequence as it pertains to FRX-L. Refer to Fig. 5 for details.

The bias bank, with a quarter cycle time,  $t_{1/4}$ , equal to 140  $\mu$ s, produces the low-level slowly-varying magnetic field which later becomes trapped to form the FRC. When the bias bank discharge is initiated, a static fill of D<sub>2</sub> gas is present in the quartz tube. Upon reaching the first minimum of the bias field, the PI bank is triggered, with  $t_{1/4} = 1.0$   $\mu$ s. This bank is used to ionize the gas by ringing the magnetic field at high frequency. We chose this pre-ionization method, known as the  $\theta$ -PI method, from among the various possibilities[2] due to its simplicity—no additional hardware except for the bank is necessary on the experiment—and cleanliness—the only impurities possible are due to the quartz tube interacting with the plasma (a transient effect occurring during PI field zero-crossing or main bank field reversal).



Once the bias field has diffused into the plasma sufficiently (determined empirically), such that the field lines are frozen into the plasma, the main bank is triggered. This bank ( $t_{1/4} = 3 \mu\text{s}$ ) is connected such that its field is opposite in direction to the original bias field, and is  $\approx 10$  times larger in magnitude than the bias field. The plasma is pulled radially outwards due to  $\mathbf{J} \times \mathbf{B}$  forces between the large induced azimuthal current and the frozen-in bias field. As the reversal field diffuses into the surface of the plasma, the force reverses direction and the outside of the plasma begins contracting radially. Soon afterwards, the fields reconnect near the ends of the theta coil, and field line tension at these locations causes the plasma to compress axially. The equilibrium FRC consists of a region of closed field lines and a region of open field lines, with the separatrix delineating the boundary between the two.

The cusp/mirror coils, located at either end of the theta coil, create a null with respect to the bias field, and seed the reconnection to occur repeatably in the same location. They also make a mirror magnetic field with respect to the main bank field, thereby holding the FRC centered underneath the theta coil after formation.

#### D. Control and Data Acquisition Systems

Control and data acquisition systems are operated from within our screen room, an rf-shielded room containing six racks of digitizers, control system components, and remote (fiber-optically connected) diagnostics. Three live video screens supply views of the experimental area to the operator and other personnel in the screen room. Other computer terminals make it possible for investigators to view and analyze data after each shot.

No hard connection exists between the experiment and the screen room. Any diagnostic signals coming into the screen room are not allowed to contact the experiment. Diagnostics that require contact with any part of the experiment are situated inside a separate rf-shielded enclosure which is allowed to float up in potential along with the experiment. Communication with these digitizers is done using a National Instruments GPIB fiber-optic extender.

The control system is comprised of air and fiber-optic signal lines which return interlock status signals and send out charge and fire signals, among others. The automatic *safing* sequence (sequence that returns the capacitor banks to a safe state) is also controlled in

this manner. The system is run on LabVIEW on a PC communicating with a National Instruments PXI crate.

The data acquisition system is run separately from the control system. The system interface was written in LabVIEW as well, but is run on a UNIX platform. Communication between the computer and the digitizers is done via GPIB bus. We use all available GPIB communication ports, i.e. 15, totaling 58 data channels at present. Digitizers range from old Camac-style LeCroy TR8818A transient recorders to VXI digitizers (HP E1427A and Tektronix TVS641A waveform analyzers). Scopes are used for data that might indicate to personnel whether or not the shot should be recorded, as the data retrieval process lasts about 5 min and is one of the limiting factors for our shot rate. The initialization/configuration information and data are stored on Sybase [30] and MDS+ [31] databases, respectively, though we will be transferring the configuration parameters to MDS+ as well. The data can be later analyzed using either IDL [32] or DWScope [31].

## E. Diagnostics

In this section we introduce the principal diagnostics utilized on FRX-L, summarized in Table II. Specific data obtained with each is discussed in Sec. III.

Magnetic field probes ( $\dot{B}$  probes) and flux loops placed in the radial gap between the discharge tube and the theta coil measure the excluded flux as a function of time [33]. The 36-cm long FRX-L theta coil is split into four equal segments, labeled A to D, each 8.25 cm long, with a 1 cm gap between them. As shown in Fig. 6, four magnetic probe/loop pairs were located at one edge of each of these segments, or at  $z = -9.25, -0.5, 8.75$ , and  $18.0$  cm, with the midpoint of the theta coil taken to be  $z = 0$ . Magnetic field probes measure the axial magnetic field at specific points, while flux loops measure the flux through the theta coil at given axial locations. The excluded flux is defined as the amount of magnetic flux (determined by the field measured with a magnetic probe and assuming azimuthal symmetry) excluded by the FRC, i.e. the flux which would be present inside the FRC separatrix if the FRC were not present. This last statement can be expressed in the form of an equation,

$$\phi_{exc} = B_p \pi r_s^2, \quad (2)$$

where  $B_p$  is the axial magnetic field measurement during a plasma shot and  $r_s$  is the FRC

separatrix radius. The relationship between the flux and magnetic probe measurements during a plasma shot can be written as

$$\phi_p = B_p \pi (r_c^2 - r_s^2), \quad (3)$$

where  $r_c$  is the inner radius of the theta coil, and  $\phi_p$  is the flux probe measurement during a plasma shot. During a vacuum shot, instead, as there is no excluded flux,

$$\phi_v = B_v \pi r_c^2, \quad (4)$$

where  $B_v$  and  $\phi_v$  are the magnetic field and flux probe measurements during a vacuum shot. Taking the ratio of these last two equations, we can obtain the separatrix radius as a function of time in terms of measured quantities:

$$r_s = r_c \left( 1 - \frac{\phi_p B_v}{\phi_v B_p} \right)^{1/2}. \quad (5)$$

The magnetic probe design is limited by both the high voltage environment in which it must operate and the narrow gap inside of which it must fit ( $\approx 5$  mm exists between the discharge tube and the theta coil).

The magnetic probe and flux loop signals are also combined into a differential integrator circuit (same one used by the University of Washington Group on the LSX experiment [34]) to provide investigators with an immediate excluded flux measurement. The magnetic probe signal is subtracted from the flux loop signal after being integrated. The flux loop signal is attenuated such that the two cancel out during a vacuum shot. A non-zero signal then indicates excluded flux is present.

The multi-chord He-Ne (632.8 nm) laser single-pass interferometer was designed by AFRL. It was originally set up with two chords, but has recently been upgraded to eight. Abel inversion and tomographic analysis of the data will provide a density plot of a cross-section of the plasma as a function of time. Originally, the interferometer was set up at the midplane of the theta coil (Fig. 6,  $z = 0$ ) with the two chords at a distance of  $r = 0$  cm and  $r = 2$  cm from the  $z$ -axis, respectively. Presently, the eight chords are set to span most of the discharge tube radius ( $z = 0, r = 0, 0.7, 1.9, 2.4, 3.0, 3.4, 3.6, 4.2$  cm). Combining the line-integrated density measured along a diameter ( $r = 0$  chord) with the excluded flux radius measurement,  $r_s$ , one can define an average density  $\langle n \rangle = \int n dr / 2r_s$ . The volume-averaged  $\beta$  can be obtained from  $x_s = r_s / r_c$  using [2],

$$\langle \beta \rangle = 1 - x_s^2 / 2. \quad (6)$$

This equation is a simple but extremely useful relation between the separatrix radius and  $\langle \beta \rangle$ , obtained by considering axial equilibrium and radial pressure balance, where axial equilibrium refers to axial force balance between field-line tension and plasma pressure (neglecting the pressure outside the separatrix and assuming the theta coil is sufficiently long such that there is a region of straight field lines in the vacuum region at either end). Assuming radial pressure balance at the midplane, one may then estimate the total plasma temperature using  $\langle \beta \rangle = n(T_e + T_i)/(B_{ext}^2/2\mu_0)$  (with  $T$  in units of eV), where  $B_{ext}$  is the magnetic field external to the FRC (measured by the magnetic probes).

Another important diagnostic is the multi-point Thomson scattering system, used to measure  $T_e$  and  $n_e$ . A 20 J pulsed ruby laser is fired through the plasma from one end at an angle such that it cuts through the high density regions of the FRC. The collecting optics, arrayed along the  $z$ -axis, are brought up close to the discharge tube by drilling holes in the theta coil. There are a total of six collectors, each viewing the plasma at three spatial points, thereby providing data at different axial and radial locations. The system is presently in its testing phase and first data is expected shortly.

### III. INITIAL RESULTS

#### A. Pre-Ionization

We utilize the  $\theta$ -PI technique to pre-ionize the gas, which consists of ringing the theta pinch coil at a high frequency, thereby inducing a large azimuthal  $E$  field which breaks down the gas.

The  $\theta$ -PI technique has both advantages and disadvantages over other methods. This method is very clean, as no electrodes are required inside the discharge tube. It also provides a high level of ionization, about 100%. The main disadvantage of this method is that it traps only  $\approx 45\%$  [35] of the initial bias field, at best. It also puts additional restrictions on the capacitor banks, as the PI bank must have at least enough voltage to cancel out the bias bank (zero crossing) as explained below [36–40].

The PI bank is fired at the first minimum of the bias field. The large azimuthal electric field induced ionizes the  $D_2$  gas. Ionization occurs initially at locations where the magnetic field is zero, or where the PI field cancels out the existing bias field (the mean free path

of the electrons is maximized at these locations). As  $E$  is proportional to  $r$ , the plasma sheath forms initially near the quartz tube wall. As the PI field oscillates, this sheath is compressed towards the axis and expanded towards the tube wall, ionizing the remaining gas via the snow-plow effect [41, 42]. The bias field diffuses into the plasma, eventually becoming trapped in it.

The more times the PI field rings, the more time the bias field has to diffuse into the plasma, although this means the plasma is expanded against the quartz tube wall more times, picking up more impurities. For this reason, the number of PI rings required before the firing of the main bank, even the exact phase of the ring where one does it, is a value determined empirically for each FRC device.

We studied the dependence of the ionization fraction on fill pressure, relative voltage of PI to bias, and variation in PI frequency (by changing the number of capacitors).

## B. FRC formation

The following are initial results on FRC formation obtained with the FRX-L device. Operation with and without cusp/mirror coils and problems with the crowbar-induced field modulation are also discussed.

Reproducible formation of FRC plasmas was difficult until we began operating with cusp/mirror coils at either end of the theta coil. Without the cusp coils, the field null points occur well outside of the theta coil, where field reconnection is more difficult due to decreased ionization levels. Reconnection without cusp coils was therefore most probably due to tearing of the field lines under the theta coil, making it very irreproducible. With the cusp coils, the field nulls occur much closer to the theta coil, and the x-points form where these nulls occur. In addition, as detailed in Sec. II C, the cusp coils form a mirror field with respect to the crowbarred main field, helping maintain the FRC inside the theta coil after formation. Without this mirror field, and with the compression due to the modulation on the crowbarred field (more below), the FRCs were ‘squeezed out’ and translated as soon as they were formed.

We present the results from a representative shot (1525; 25.3 mTorr  $D_2$  static fill) which exhibits good lifetime and an  $n = 2$  rotational instability, a characteristic particular to FRCs [43]. Though the actual cause of the rotation of this instability is still a matter of

debate, the mode is well characterized. The cross-section of the FRC is elongated along one direction, taking an oval rather than circular shape. The FRC then rotates, its cross-section eventually elongating enough to skim the walls of the container, quickly losing containment.

Figure 7 shows a plot of the axial magnetic field measured with the probe from theta coil segment A (refer to Fig. 6) along with plots of the excluded flux, line-integrated density (left column), and various calculated quantities (right column). The density was measured at  $z = 0$ ,  $r = 0, 2$  cm, using the two-chord version of the visible HeNe interferometer. The volume-averaged beta  $\langle \beta \rangle$ , normalized separatrix radius  $x_s$ , and  $T_e + T_i$  are calculated as detailed in Sec. II E. The  $B$  plot shows the initial negative bias magnetic field and the PI field superimposed at  $t \approx 1 \mu\text{s}$ . The main (reversed) field is fired just before the PI completes 1.5 cycles. The field reaches a maximum at  $9.5 \mu\text{s}$ , after which point it oscillates dramatically due to the effect of the crowbar inductance in the circuit. Ideally one desires a monotonically decaying field after reaching this peak. The vertical dashed lines refer to times at which excluded flux is calculated in Fig. 8. The excluded flux was obtained at the same axial location as the bottom plot. The bottom left plot shows the initial line-integrated electron density at  $z = 0$  as the gas is ionized, followed by a sudden increase during field reversal. The density becomes quiescent from  $\approx 12 \mu\text{s}$  until about  $15 \mu\text{s}$ , when it begins to oscillate, as is characteristic of FRCs undergoing an  $n = 2$  instability. The off-axis chord does not traverse through any plasma when the major radius of this ellipse is along the direction of the interferometer beam, while the density in the off-axis chord is maximized when the FRC has rotated by a further 90 degrees. As shown on the plots on the right column, the FRC is formed at  $\approx 10 \mu\text{s}$  with an  $x_s = 0.29$ ,  $T_e + T_i = 440$  eV, and  $\langle n_e \rangle = 3.9 \times 10^{16} \text{ cm}^{-3}$ . It reaches an equilibrium state at  $\approx 12 \mu\text{s}$ , with  $x_s = 0.43$ ,  $T_e + T_i = 250$  eV, and  $\langle n_e \rangle = 1.3 \times 10^{16} \text{ cm}^{-3}$ .

The error on the magnetic field and line-integrated density plots are less than the line width on the scale shown. To obtain the  $\phi_{exc}$  plot, a single point measurement is used to obtain the magnetic field and symmetry is assumed (which does in fact turn invalid once the plasma becomes asymmetric, after onset of the  $n = 2$  instability). The derived quantities on the right column of the figure are obtained as detailed in the diagnostic section and using values from the left column. Because the excluded flux becomes invalid after asymmetry sets in, so are these derived values ( $\langle \beta \rangle$ ,  $x_s$ , and  $T_e + T_i$ ), which depend on the  $\phi_{exc}$  measurement. Therefore, the values on the right column should be ignored after instability

sets in (cross-hatched portion).

The excluded flux (or separatrix) radius is obtained as detailed in Sec. II E. By using probes at the four locations indicated above, we obtain the excluded flux radius for the same shot shown in Fig. 7. The separatrix radius  $r_s$  oscillates with the same frequency as the crowbarred field, increasing in size when the field gets weaker and vice versa. One can use this radius to obtain the excluded flux by multiplying the excluded area ( $\pi r_s^2$ ) times the external field measured by the magnetic probes. The excluded flux radius can be calculated at the four locations indicated above, as a function of time. These values are then splined along  $z$ , and smoothed in time, and combined to obtain a contour plot of the excluded flux vs time, as shown in Fig. 8. This figure shows, via the excluded flux, the FRC separatrix forming and monotonically diminishing in length and losing excluded flux, even with the crowbarred field oscillating to less than 50% of its original value. The top plot in this figure is a contour plot showing the magnitude of the excluded flux (mWebers) as a function of  $z$  position and time. The bottom plot shows the excluded flux vs  $z$  at various times, obtained by taking cross-sections of the contour plot at the times indicated on it with dashed lines. Note that these are the same times that were labeled in Fig. 7. The markers indicate actual data points at the probe locations. The same arguments regarding the validity of  $\phi_{exc}$  in Fig. 7 apply to this figure.

#### IV. FUTURE DIRECTIONS

We are currently working on solving the problem of the excessive modulation in the crowbarred magnetic field. As this containing field oscillates, the FRC increases and decreases in radius, running the risk of hitting the walls; it also stretches axially, possibly beyond the ends of the theta coil, into regions of cold un-ionized gas. Possible solutions for the crowbar ringing problem include reducing the inductance of the crowbar switch, increasing the load inductance, and operating at higher main bank voltages, resulting in better rail gap conduction (and possibly also lower switch inductance).

Initial results and comparison to older published results gives us confidence that the device is performing near expectations. These results are exciting indications of the potential performance of the device, and the confirmation of these estimates with more direct measurements (Thomson scattering) is anticipated. We are well on our way to achieving the

parameters required to make an MTF target FRC. Table III shows important parameters and values achieved so far, along with required values ( $\phi_{equil}$  is calculated as in [24], using  $\epsilon = 0.25$ ). Increasing bank voltages and hardware modifications should allow us to push further into the parameter space.

## Acknowledgments

The authors would like to thank J.C. Cochrane, M.C. Thomson, G. Parker, R. Gribble, F.J. Wysocki, J. Faulkner, R. Newton, and the University of Washington FRC team for the guidance and help they provided, and to acknowledge the technical support of D. Begay, E. Mignardot, G. Sandoval, and B. Martinez. This work was supported by DOE-OFES contract W-7405-ENG-36.

- 
- [1] G. A. Wurden, K. F. Schoenberg, R. E. Siemon, M. Tuszewski, F. J. Wysocki, and R. D. Milroy, in *Proceedings of the 9th International Toki Conf. on Plasma Physics and Controlled Nuclear Fusion* (Toki, Japan, 1998), p. 238.
  - [2] M. Tuszewski, Nucl. Fusion **28**, 2033 (1988).
  - [3] D. J. Rej, R. D. Milroy, M. Tuszewski, R. E. Siemon, E. G. Sherwood, K. F. McKenna, R. K. Linford, P. L. Klingner, R. E. Chrien, and W. T. Armstrong, Phys. Fluids **29**, 852 (1986).
  - [4] J. Lindl, Phys. Plasmas **2**, 3933 (1995).
  - [5] J. G. Linhart, H. Knoepfel, and C. Gouylan, Nucl. Fusion **1962 Supplement, Part 2**, 733 (1962).
  - [6] R. E. Siemon, I. R. Lindemuth, and K. F. Schoenberg, Comments Plasma Phys. Control. Fusion **18**, 363 (1999).
  - [7] I. R. Lindemuth, R. E. Reinovsky, R. E. Chrien, J. M. Christian, C. A. Ekdahl, J. H. Goforth, R. C. Haight, G. Idzorek, N. S. King, R. C. Kirkpatrick, et al., Phys. Rev. Lett. **75**, 1953 (1995).
  - [8] R. C. Kirkpatrick, I. R. Lindemuth, and M. S. Ward, Fusion Technology **27**, 201 (1995).
  - [9] S. Glasstone and R. H. Lovberg, eds., *Controlled Thermonuclear Reactions* (D. Van Nostrand, 1960).



- [10] J. M. Taccetti, T. P. Intrator, F. J. Wysocki, K. Forman, D. Gale, S. Coffey, and J. H. Degnan, *Fusion Sci. Tech.* **41**, 13 (2002).
- [11] T. P. Intrator, J. M. Taccetti, D. A. Clark, J. H. Degnan, D. Gale, S. Coffey, P. Rodriguez, W. Sommars, B. Marshall, F. J. Wysocki, et al., *Nucl. Fusion* **42**, 211 (2002).
- [12] J. H. Degnan, J. M. Taccetti, T. Cavazos, D. Clark, S. K. Coffey, R. J. Faehl, M. H. Frese, D. Fulton, J. C. Gueits, D. Gale, et al., *IEEE Trans. Plasma Sci.* **29**, 93 (2001).
- [13] R. E. Reinovsky, W. L. Baker, Y. G. Chen, J. Holmes, and E. A. Lopez, in *Digest of Technical Papers: IEEE Fourth International Pulsed Power Conference* (Albuquerque, NM, 1983), p. 196.
- [14] W. M. Parsons, E. O. Ballard, R. R. Bartsch, J. F. Benage, G. A. Bennett, R. L. Bowers, D. W. Bowman, J. H. Brownell, J. C. Cochrane, H. A. Davis, et al., *ieeeplasma* **25**, 205 (1997).
- [15] A. Eberhagen and W. Grossmann, *Z. Phys.* **248**, 130 (1971).
- [16] A. C. Kolb, W. H. Lupton, R. C. Elton, E. A. McLean, M. Swartz, M. P. Young, H. R. Griem, and E. Hintz, in *Plasma Physics and Controlled Nuclear Fusion Research (Proc. 2nd Int. Conf. Culham, 1965)* (1966), p. 261.
- [17] E. A. McLean, A. D. Anderson, and H. R. Griem, in *Topical Conference on High Beta Plasma, Los Alamos, NM* (1967).
- [18] A. Kaleck, H. Kever, L. Könen, P. Noll, K. Sugita, F. Waelbroeck, and H. Witulski, in *Topical Conference on High Beta Plasma, Los Alamos, NM* (1967).
- [19] A. Kaleck, L. Könen, P. Noll, K. Sugita, F. Waelbroeck, K. Watanabe, and H. Witulski, in *Plasma Physics and Controlled Nuclear Fusion Research (Proc. 3rd Int. Conf. Novosibirsk, 1968)* (1969), p. 581.
- [20] G. A. Wurden, T. P. Intrator, D. A. Clark, R. J. Maqueda, J. M. Taccetti, F. J. Wysocki, S. K. Coffey, J. H. Degnan, and E. L. Ruden, *Rev. Sci. Instrum.* **72**, 552 (2001).
- [21] G. A. Wurden, *Fusion Eng. Design* **34-35**, 301 (1997).
- [22] D. J. Rej and M. Tuszewski, *Phys. Fluids* **27**, 1514 (1984).
- [23] W. T. Armstrong and J. A. Morgan, in *Megagauss Technology and Pulsed Power Applications* (1987), p. 683.
- [24] M. Tuszewski, *Phys. Fluids* **31**, 3754 (1988).
- [25] D. J. Rej, G. A. Barnes, R. J. Gribble, J. E. Hinckley, T. W. Kreider, and W. J. Waganaar, *Tech. Rep., Los Alamos National Laboratory Report LA-11519-MS* (1989).

- [26] R. E. Siemon, W. T. Armstrong, D. C. Barnes, R. R. Bartsch, R. E. Chrien, J. C. Cochrane, W. N. Hugrass, J. R. W. Kewish, P. L. Klingner, H. R. Lewis, et al., *Fusion Technology* **9**, 13 (1986).
- [27] W. J. Waganaar, J. C. Cochrane, K. W. Hosack, T. P. Intrator, P. G. Sanchez, J. M. Taccetti, M. C. Thompson, and C. Grabowski, Tech. Rep., Los Alamos National Laboratory Report LA-UR-02-7660 (2002), als submitted to Proceedings of 2003 IEEE Pulsed Power Conference.
- [28] C. Grabowski, J. H. Degnan, T. Cavazos, D. G. Gale, C. Gilman, W. Sommars, T. P. Intrator, J. M. Taccetti, W. Waganaar, R. E. Siemon, et al., *IEEE Trans. Plasma Sci.* **30**, 1905 (2002).
- [29] A. L. Hoffman, R. D. Milroy, J. T. Slough, and L. C. Steinhauer, *Fusion Technology* **9**, 48 (1986).
- [30] *Adaptive Server Enterprise 12.5 Reference Manual*, Sybase (2002).
- [31] J. A. Stillerman, T. W. Fredian, K. A. Klare, and G. Manduchi, *Rev. Sci. Instrum.* **68**, 939 (1997).
- [32] *IDL Reference Guide*, Research Systems (2002).
- [33] M. Tuszewski, *Phys. Fluids* **24**, 2126 (1981).
- [34] A. L. Hoffman, L. N. Carey, E. A. Crawford, D. G. Harding, T. E. Dehart, K. F. McDonald, J. L. McNeil, R. D. Milroy, J. T. Slough, and R. Maqueda, *Fusion Technology* **23**, 185 (1993).
- [35] W. T. Armstrong, J. C. Cochrane, R. J. Commiso, J. Lipson, and M. Tuszewski, *Appl. Phys. Lett.* **38**, 680 (1981).
- [36] G. B. F. Niblett and T. S. Green, *Proc. Phys. Soc.* **74**, 737 (1959).
- [37] H. Kever, *Nucl. Fusion* **1962 Supplement, Part 2**, 613 (1962).
- [38] T. S. Green, *Nucl. Fusion* **2**, 92 (1962).
- [39] T. S. Green and A. A. Newton, *Phys. Fluids* **9**, 1386 (1966).
- [40] R. J. Commiso, W. T. Armstrong, J. C. Cochrane, C. A. Ekdahl, J. Lipson, R. K. Linford, E. G. Sherwood, R. E. Siemon, and M. Tuszewski, in *Proceedings of the Third Symposium on the Physics and Technology of Compact Toroids in the Magnetic Fusion Program* (1980), p. 184.
- [41] M. Rosenbluth, R. Garwin, and A. Rosenbluth, Tech. Rep., Los Alamos National Laboratory Report LA-1850 (1954).
- [42] M. Rosenbluth, *Magnetohydrodynamics* (Stanford University Press, Stanford, 1957), p. 57.
- [43] S. Ohi, T. Minato, Y. Kawakami, M. Tanjyo, S. Okada, Y. Ito, M. Kako, S. Goto, T. Ishimura,

and H. Ito, Phys. Rev. Lett. **51**, 1042 (1983).

## Tables

TABLE I: FRX-L Experimental Parameters

Parameter	Design	Achieved
<i>FRC plasma</i>		
density	$10^{17} \text{ cm}^{-3}$	$\approx 1\text{--}8 \times 10^{16} \text{ cm}^{-3}$
temperature $T_i, T_e$	50–300 eV	$T_e + T_i \approx 250\text{--}400 \text{ eV}$
radius (separatrix)	2.8 cm	2.8 cm
length	30 cm	$\approx 30 \text{ cm}$
peak compression field	4 T	3 T
energy confinement time	25 $\mu\text{s}$	$> 10 \mu\text{s}$ (equil phase)
<i>Hardware</i>		
coil radius, $r_c$	6.2 cm	6.2 cm
coil length, $l_c$	36.0 cm	36.0 cm
coil voltage	39 kV	37 kV
reversal electric field	1 kV/cm	0.95 kV/cm
main field risetime	2.5 $\mu\text{s}$	2.5 $\mu\text{s}$
D <sub>2</sub> fill pressure, $p_0$	80 mTorr	30–80 mTorr
lift-off field	0.7 T	0.15 T

TABLE II: FRX-L Diagnostics

<b>Diagnostic</b>	<b>Information provided</b>
<i>Present:</i>	
Flux loops, $B_z$ probes	separatrix radius, excluded field
Multi-chord He-Ne red interferometer (single-pass), side-on	density
Optical tomography	large-scale plasma behavior
Framing camera, end-on	large-scale plasma behavior
Bolometer	radiated power
Multi-channel spectrometer	impurity line intensities vs time
<i>Undergoing initial testing:</i>	
Multi-point Thomson scattering	$T_e, n_e$

TABLE III: FRX-L Summary of Experimental Results

Parameter	Before Contraction (at 10 $\mu s$ )	Equilibrium Value (at 12 $\mu s$ )	Desired Value
$\langle n_e \rangle$ ( $\text{cm}^{-3}$ )	$\approx 3.9 \times 10^{16}$	$\approx 1.3 \times 10^{16}$	$(1-10) \times 10^{17}$
$T_e, T_i$ (eV)	$T_e + T_i \approx 440$	$T_e + T_i \approx 250$	50–300
$\phi_{equil}$ (mWebers)	N/A	0.3	1.0

## Figures



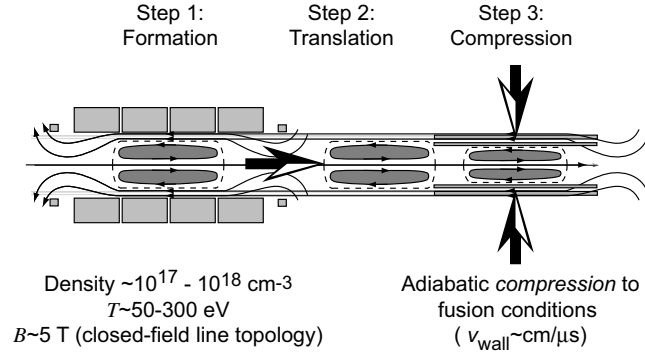


FIG. 1: The three steps of FRC-based MTF.

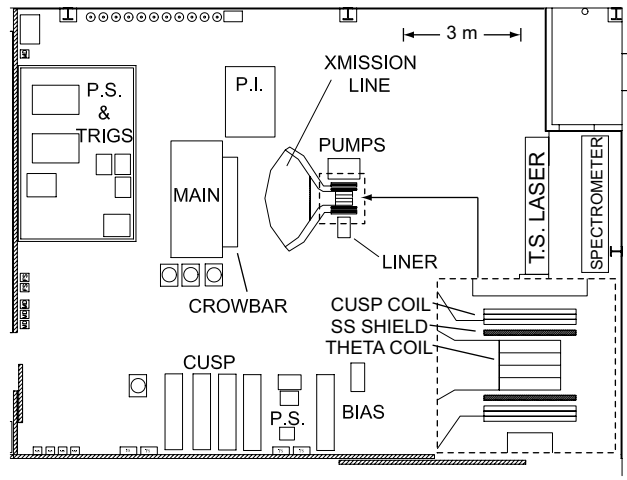


FIG. 2: Layout of FRX-L components, including main, bias, pre-ionization (P.I.), and cusp capacitor banks, transmission (xmission) line, power supplies (P.S.), triggers (trigs), stainless steel (SS) shields, theta coils, cusp coils, and liner. (Inset is a closeup of the device central core.)

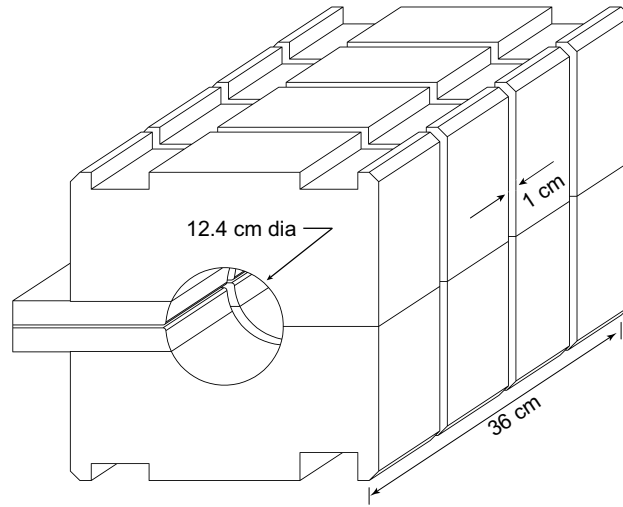


FIG. 3: Detailed schematic of FRX-L theta-coil.

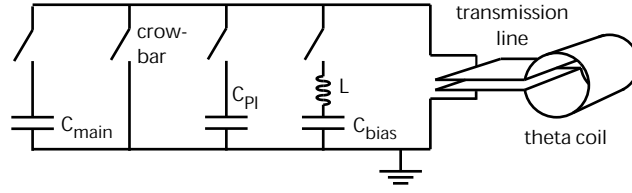


FIG. 4: Simplified electrical circuit of the FRX-L device.

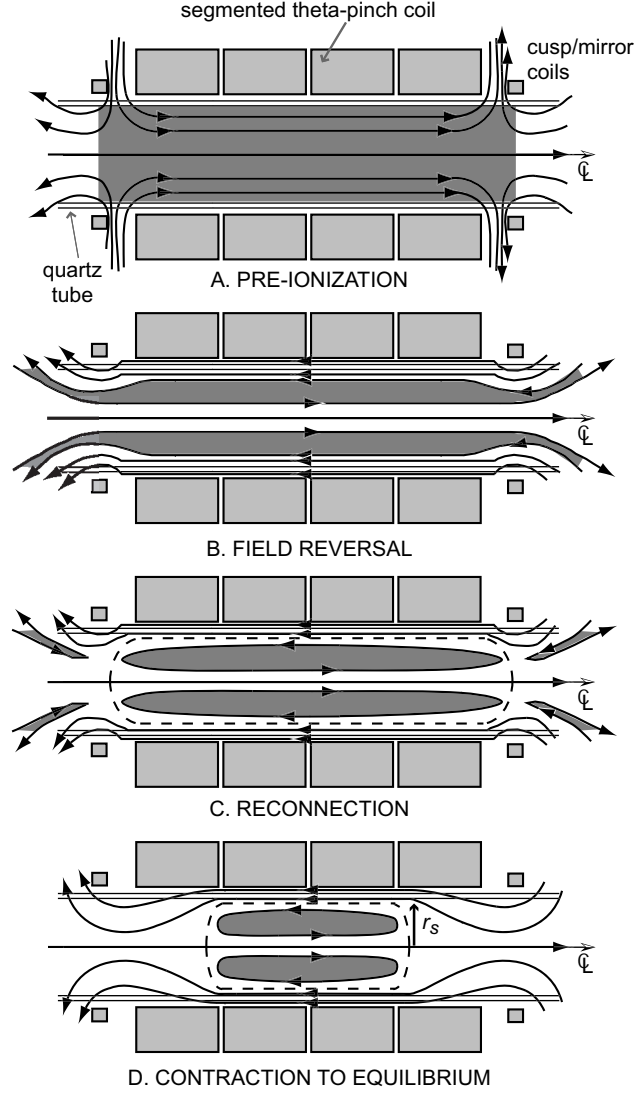


FIG. 5: FRC formation sequence, from top to bottom: A. Chamber is filled with neutral gas, bias magnetic field is applied, and gas is ionized; B. Current in theta pinch coil is rapidly reversed, plasma implodes; C. Magnetic field lines reconnect; D. FRC contracts axially to equilibrium configuration (separatrix radius  $r_s$  is shown).

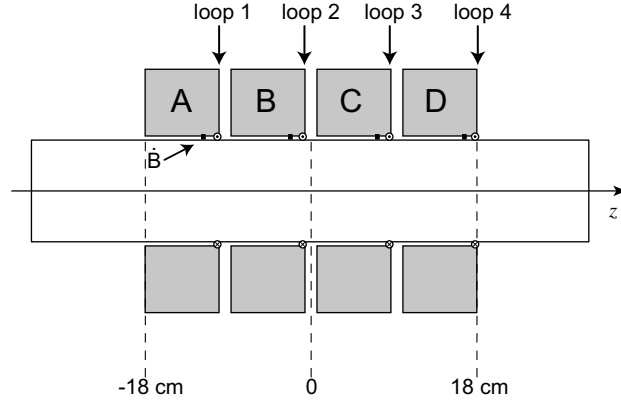


FIG. 6: Cross-section of theta-coil showing location of flux loop and  $\dot{B}$  probes.

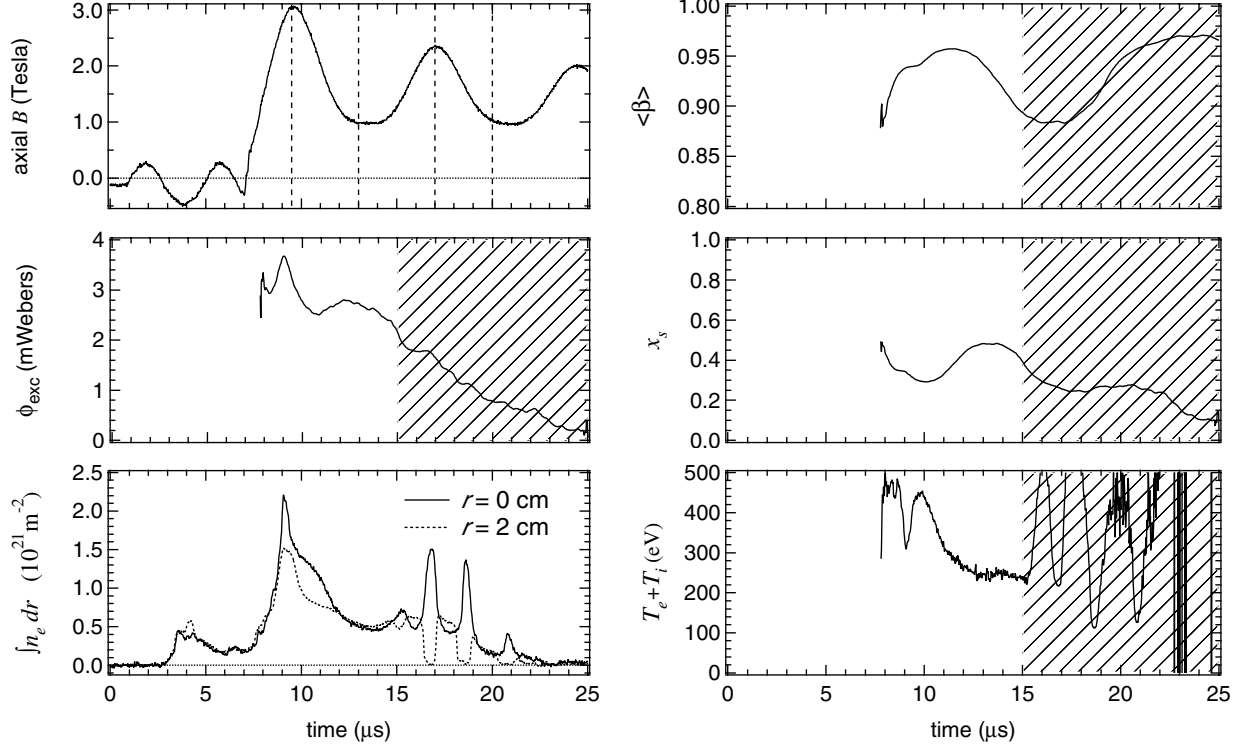


FIG. 7: Correlation between axial magnetic field, excluded flux, and integrated line density (left column), and calculated quantities volume-averaged beta  $\langle \beta \rangle$ , normalized separatrix radius  $x_s$ , and  $T_e + T_i$  (right column), FRX-L shot 1525. Crowbar mismatch is evident in the  $B$  plot after peak field. The vertical dashed lines in this plot refer to times at which excluded flux is calculated in Fig. 8. Integrated line density is shown at two radii. Plasma density persists beyond the first crowbar modulation cycle but undergoes characteristic  $n = 2$  instability after  $15 \mu\text{s}$ . Cross-hatched portions indicate where FRC symmetry assumption used in deriving those quantities becomes invalid.

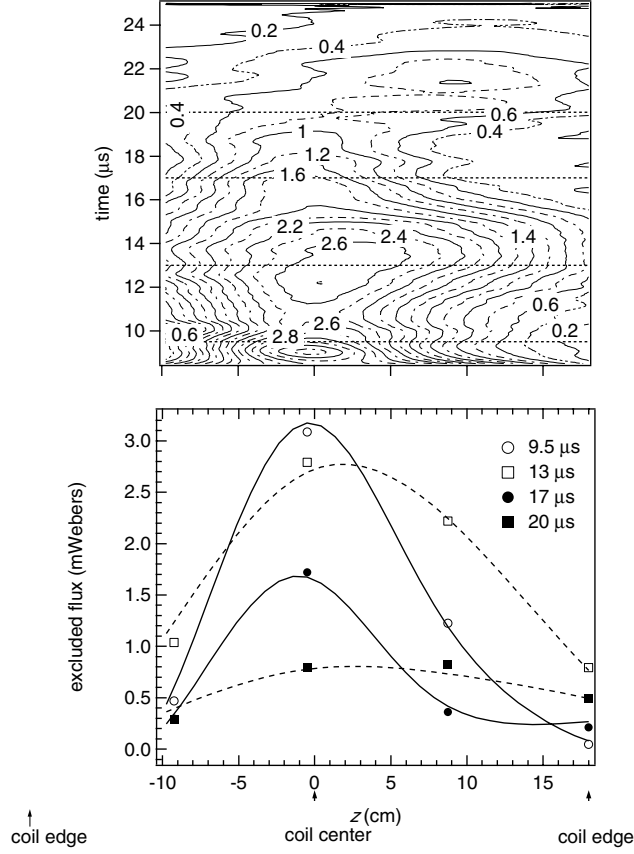


FIG. 8: Excluded flux contours as a function of time and axial position, FRX-L shot 1525 (top), and excluded flux vs axial position at various times (bottom). Lineouts at 9.5  $\mu\text{s}$  and 13  $\mu\text{s}$  correspond to the first peak in the main reversal field and the first minimum of the modulation, respectively (see Fig. 7). Data points (markers) are splined along  $z$ .